Progress in developing PICTURE-D Polarimeter: a polarimeter for characterizing debris disk properties

Guangfeng Yu[a], Christopher Mendillo[a], and David Doelman[b]

[a]UMass Lowell, Lowell center for space science technology, Physics Department, 650 Suffolk Street, Lowell, MA, USA
[b]SRON Space Research Organisation Netherlands, Niels Bohrweg 4, Leiden, South Holland, Netherland

ABSTRACT

We present progress in the development of the PICTURE-D polarimeter, an auxilliary optical instrument of the Planetary Imaging Coronagraph Testbed Using a Recoverable Experiment Debris Disk (PICTURE-D) mission designed for the purpose of characterizing debris disk properties. There are several technical milestones we want to achieve with this polarimeter: 1. We intend to measure both orthogonal polarization states on the sky simultaneously, something that was limited by PICTURE-D's predecessor PICTURE-C due to polarization leakage filtering. 2. We intend to use phase-diversity in the polarization images to perform electric field aberration retrieval in the pupil plane, based on existing literature that describes the algorithm and theory. In this manuscript we describe the progress we have made regarding building the polarimeter and our attempts to implement the polarization phase diversity based wavefront sensing.

Keywords: Optics, Coronagraph, VVC, Polarimeter, EFC

1 Introduction

The Planetary Imaging Coronagraph Testbed Using a Recoverable Experiment for Debris Disks (PICTURE-D) mission is a balloon-borne suborbital research program to directly image several debris disks around nearby stars in reflected visible light. The mission aims to characterize disk morphology, constrain dust grain properties, examine planet-dust interactions and calibrate dust models for future exoplanet imaging missions.

A successor of the previous PICTURE-C (Planetary Imaging Coronagraph Testbed Using a Recoverable Experiment Coronagraph) mission, PICTURE-D intends to demonstrate several new technologies that can potentially improve debris disk characterizations. One of the new technologies we will develop for PICTURE-D is polarimetry. Debris dust properties are notoriously degenerate.[1] As previous research has shown,[2] the implementation of the polarimetric modality will help us constrain the properties of the debris disk such as the shape, compositions and size of the disk. We aim to integrate polarimetry into the PICTURE-D optical design so that we can extract the total intensity and polarized scattering phase functions (SPF) from the polarization measurement of the debris disk, and use them to study dust grain properties. The goal of PICTURE-D's polarimetric system is to measure both orthogonal linear polarization states simultaneously at high contrast in the order of 10^{-7}. Additionally, we also want to explore the possibilities of using the pair of measurement images to perform polarization based wavefront aberration estimation and correction without implementing focal plane wavefront probing.[3] Directly using the measurement images to perform wavefront sensing increases the efficiency of dark zone convergence by a factor of four since we are not acquiring the additional four images for pair-wise probing. A scheme of utilizing the dual polarization states to retrieve wavefront aberration is presented in the theoretical and computational studies done by P. Riaud et. al.[4] In this study they demonstrated that with the Nijboer-Zernike theory of diffraction it is possible to derive wavefront aberrations in the pupil plane in the form of Zernike polynomials from a pair of orthogonally polarized images. We implemented this method and would discuss the results later in the article.

Further author information: (Send correspondence to Guangfeng Yu.)
Guangfeng Yu: E-mail: Guangfeng_Yu@student.uml.edu, Telephone: +1 413 801 8376
Christopher Mendillo.: E-mail: Christopher_Mendillo@uml.edu

Techniques and Instrumentation for Detection of Exoplanets XII, edited by Garreth J. Ruane, Maxwell A. Millar-Blanchaer, Proc. of SPIE Vol. 13627, 1362721
2025 Published by SPIE · 0277-786X · doi: 10.1117/12.3063280

2 Polarimeter

2.1 Using Polarimeter with VVC

PICTURE-D and it's predecessor PICTURE-C uses vector vortex coronagraph (VVC) in conjunction with a wavefront control system to produce high contrast dark regions. VVC is a liquid crystal optic that is essentially a halfwave plate in which the fast optical axis rotates about the center of the optic. VVC's rotationally symmetric variation of the optical axes manipulates both the left-hand and the right-hand circularly polarized light in such a way that helical phase ramps in the azimuthal angle are embedded. The number of 2π shifts of the phase, is equivalent to the value of topological charge l_p. It should be noted that the left-hand and the right-hand circularly polarized light experience opposite phase ramp. This characteristic gives rise to a phase diversity between the two circular polarization states. At the center of the helical phase ramp a phase singularity is created. When star light collected by a telescope focuses on such phase singularity point and then propagates to a pupil plane, i.e collimating through a lens, the Fourier transform (FT) of the product of the PSF by the azimuthal phase ramp diffracts the star light outside the original pupil area and create a dark region centering around the optical axis. The diffracted star light is blocked by a lyot stop. Light from Off-axis image objects (exoplanets, debris disks) in the field of view will remain after the VVC, and can be detected with sufficient contrast.

The traditional VVC phase plate that flew on PICTURE-C is limited to operating in one circular polarization at a time. The polarization limitation is imposed due to the necessity of polarization filtering, which removes fabrication induced polarization leakage. Previously on the PICTURE-C optics the polarization leakage filtering is performed with two circular polarizers that sandwich the VVC. Since the pair of circular polarizers are aligned to opposite handedness, this polarization filtering arrangement limits the PICTURE-C to only measure one circular polarization state at a time. Studies done by Doelman et.al,[56] present a new design of VVC called double grating VVC (dgVVC) that significantly negates the polarization leakage term with extra grating layers. The dgVVC frees up the limiting circular polarizers used in polarization filtering and allows for simultanesous orthognal polarization detection. We intend to integrate dgVVC into our design as an essential part of PICTURE-D since this will increase the efficiency of our polarization measurements. Figure 1 depicts the design schematic of the polarimeter integrated Picture-D optics. In this design, a Quarter wave plate is used to first turn in sky polarized light, which can be interpreted as combinations of two orthogonal linear polarization states, into left-hand and right hand circular polarizations. Upon interactions with the dgVVC, both circular polarization states will be inverted to the other circular polarization states.[7] After the VVC, a combination of a quarter waveplate and wallaston prism is used to convert the opposite handed circular polarizations into orthogonal linear polarizations, and split up the linearly polarizaed light into two propagation paths so that they can be detected at the same time.

2.2 Polarimeter design and Demo

As a proof of concept, we have built a rotating wave plate Stokes polarimeter demo that can image and measure the polarization state of collimated laser light (see Figure 2). The polarization state of the laser light is controlled by a linear polarizer and a liquid crystal (LC) screen. This polarimeter has the capacity to measure polarization states of the beam as a global average and as local polarization measurements in each detector pixel. In this polarimeter setup, a beam expander collimates and expands the incident light. The collimated light then passes through a polarizer and a LC screen, which manipulates the polarization states of the beam. Then, the light passes through a rotating quarter waveplate, followed by a fixed linear polarizer, the combination of which is the polarimeter unit. Finally, the light is received by a detector and optical flux measurements are acquired while the waveplate rotates through 8 angles with steps of $\frac{\pi}{8}$.[9] In the case of a quarter waveplate, the flux measurement $P(\theta)$ at each waveplate angle θ is given by:

$$P(\theta) = a_0 + b_2 sin(2\theta) + a_4 cos(4\theta) + b_4 sin(2\theta) \tag{1}$$

Where the Fourier coefficients a_0,b_2,a_4, and b_4 are related to the Stokes parameters by:

$$S_0 = 2(a_0 - a_4), S_1 = 4a_4, S_3 = 4b_4, S_2 = -2b_2 \tag{2}$$

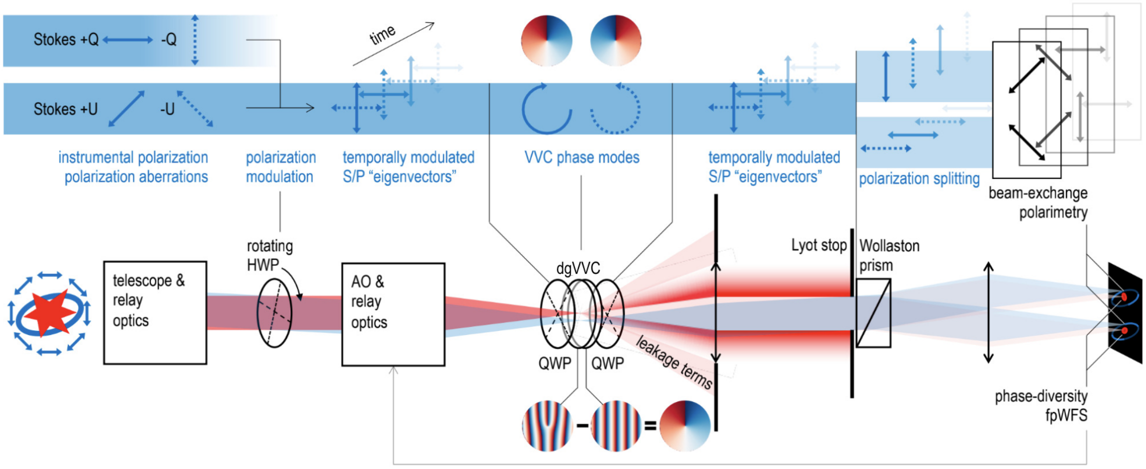

Figure 1. Polarimetry concept schematic for PICTURE-D.[8] A pair of quarter wave plates (QWPs) (center) transform linear polarization on the sky into circular polarization at the dgVVC.

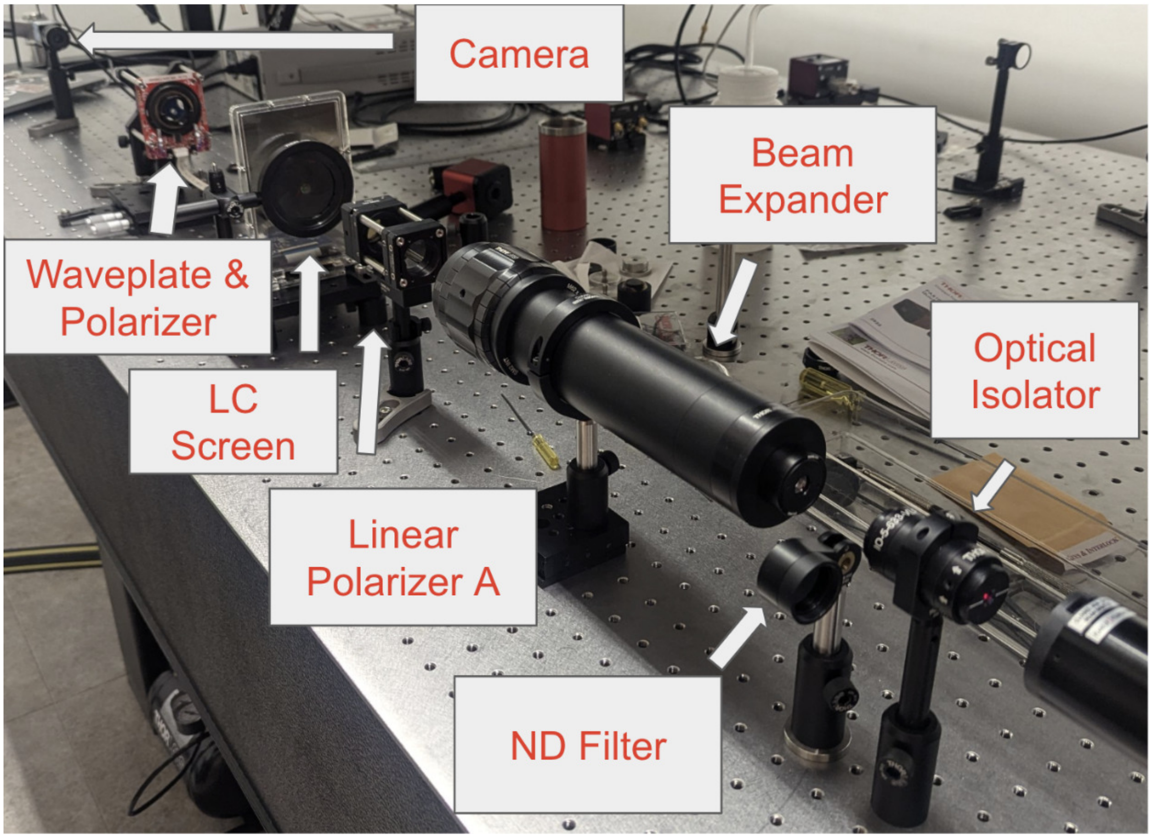

Figure 2. Polarimeter demo setup. The polarimeter is a rotating waveplate Stokes polarimeter.

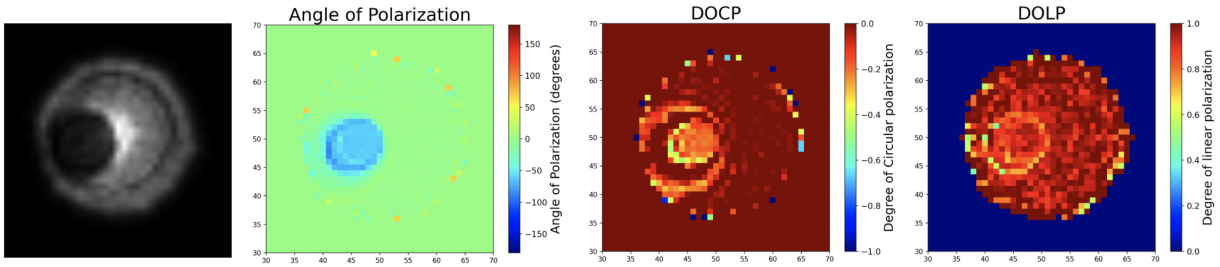

Figure 3. Polarimetric measurements. left: beam as seen on the camera. The bright area is linearly polarized with polarization axis on the horizontal axis (0 degree). The dark area is modulated by the liquid crystal screen to have elliptical polarization. The screen has liquid crystal actuators that can become active when a voltage is applied to them. Middle left: Angle of polarization measurement (AOP). Middle right: degree of circular polarization measurement (DOCP). Right: Degree of linear polarization measurement (DOLP).

Solving equation 1 and 2 with the 8 flux measurements will give us the value of Stokes parameters. Figure 3 and Figure 4 demonstrate the local and the global polarization measurements we can take with the polarimeter demo. For Figure 3, in the camera image (left), The original beam is linearly polarized while the dark region is modulated by the liquid crystal screen to have an elliptical polarization profile . The measurement plots are value maps of degree of circular polarization (DOCP, middle right), angle of polarization (AOP, middle left), and degree of linear polarization (DOLP, right). Our global measurements matches with the input, which is validated by a commercially available polarimeter (PAX1000VIS, Thorlabs).

The above mentioned measurements are defined as:

$$AOP = \frac{1}{2}\arctan\left(\frac{S_2}{S_1}\right) \tag{3}$$

$$DOCP = \frac{S_3}{S_0} \tag{4}$$

$$DOLP = \frac{\sqrt{S_1^2 + S_2^2}}{S_0} \tag{5}$$

These measurements are derived from the Stokes parameter image measurements. We emphasize here that the polarimeter demo, as it uses quarter wave plate, all 4 stokes parameters can be measured. In the case of the conceptual PICTURE-D polarimetry, as the final measurements are in linear polarization states only, we use half wave plate instead, which allows for measurements of two linear polarization related Stokes parameters: S1 and S2, but not the circular polarization related stokes parameter S3. The rotating half wave plate (HWP) modulates the polarization at four different angles to reconstruct the full linear Stokes S1 and S2 polarization vectors.

3 Polarization Wavefront Sensing

As mentioned before, the VVC imposes a spatially antisymmetric phase[10] on the left-hand and right-hand circular polarization images. This introduces a known phase diversity that can be used to perform wavefront sensing. Researchers have developed a numerical method to retrieve pupil plane electric field phase and amplitude aberrations in the Zernike basis. Compared to the focal-plane probing method employed by previous PICTURE-C mission, This wavefront sensing method has the advantage of instantaneous wavfront aberration retrieval. We present here our attempt to implement this method with simulated images.

3.1 Summary of the Riaud method

The complete mathematical derivations of the Nijboer-Zernike Polarization wavefront sensing method, developed by Riaud et.al, is presented in the original paper.[4] Here we summarize the method and the expected result. This

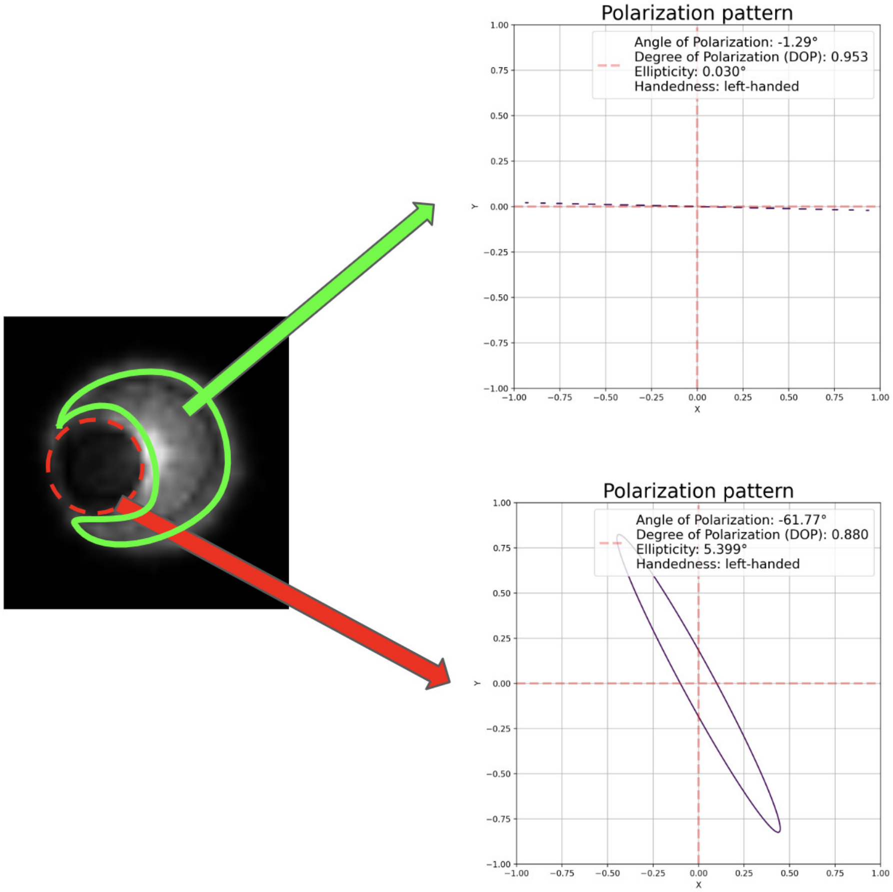

Figure 4. Polarimetric measurements showing the polarization patterns in different regions of the beam. The darker region is modulated by the LC screen and displays elliptical polarization. The bright region is linearly polarized.

method retrieves the pupil plane electric field from a set of three science image measurements: The two orthogonal linear polarization images, and a third unpolarized image, which comes from summing the two linearly polarized images. Each image corresponds to a specific topological charge value l_p, with right hand circular polarization image having $l_p = 6$, left hand circular polarization image having $l_p = -6$, unpolarized image having $l_p = 0$.

Essentially, The Riaud method represents the pupil function $P(\rho, \theta)$ as a linear system of Zernike Polynomials:

$$P(\rho, \theta) = \sum_{n,m} \beta_n^m Z_n^m = \sum (Re(\beta_n^m) + Im(\beta_n^m)) Z_n^m \tag{6}$$

Here the β_n^m is a complex coefficient. The convinience of this representation is that both the amplitude and the phase aberrations are included. The Riaud method retrieves for these complex β_n^m coefficients by solving a linear set of equations that comes from comparing the measured PSF I_{meas} and the analytically expressed PSF I_c, which is based on the complex β_n^m pupil expression:

$$I_{meas} = I_c \tag{7}$$

The method then projects both PSFs to radial template modes through means of polar Fourier transform.

$$\frac{1}{2\pi}\int_0^{2\pi} I_{meas}e^{im\phi}d\phi = \frac{1}{2\pi}\int_0^{2\pi} I_c e^{im\phi}d\phi \tag{8}$$

The analytical PSF I_c can be written as:

$$I_c = |U|^2 \tag{9}$$

Where U is the complex amplitude in the image plane with the expression:

$$U(r,\phi) = \sum_{n,m} \beta_n^m U_n^m = \sum_{n,m} \beta_n^m (\int_0^1 d\rho \int_0^{2\pi} d\theta Z_n^m(\rho,\theta) e^{-2i\pi r\rho cos(\theta-\phi)}) \tag{10}$$

As U_n^m is the image plane complex amplitude corresponding to Z_n^m. Z_n^m and U_n^m is related by the Fraunhoffer integration in equation 10.

The Riaud Method uses Bessel functions to rewrtie equation 10 and develops a modal function $V_{m,n}^{l_p}$ to represent the contribution of each Zernike mode Z_n^m after Fraunhoffer integration. Visualized examples of these Modal functions can be seen in Figure 7. Equation equation 10 then becomes:

$$U(r,\phi) = \sum_{n,m} 2i^m (\beta_{cn}^m C_m(\phi) + \beta_{sn}^m S_m(\phi)) V_{n,m}^{l_p}(r,\phi) \tag{11}$$

Where the modes are split into even cosine modes C_m and odd sine modes S_m, with corresponding β_{cn}^m and β_{sn}^m coefficeints. The analytical PSF expression, according to equation 9, is then composed of these modal functions, their coupled products, and higher order terms. The Riaud method attempts to approximate the analytical PSF to be linear by assuming the presence of a dominant mode of $V_{0,N}^{l_p}$, which also corresponds to the dominant aberration in the optical system, to be far larger than the other $V_{m,n}^{l_p}$ aberration term. As a result an approxiamtion is applied to the analytical PSF that only considers the contribution from this dominant term $V_{0,N}^{l_p}$ and a linear function $f^{(1)}$ that consists of coupled terms $V_{0,N}^{l_p} \cdot V_{m,n}^{l_p}$:

$$\frac{1}{2\pi}\int_0^{2\pi} I_{meas}e^{im\phi}d\phi \approx \frac{1}{2\pi}\int_0^{2\pi} (4(\beta_N^0(d_c))^2 |V_{N,0}^{l_p}|^2 + f^{(1)}[\beta_n^m]) e^{im\phi}d\phi \tag{12}$$

denoting the left hand side polar Fourier transformed PSF with Ψ_{meas}^m

$$\Psi_{meas}^m \approx \frac{1}{2\pi}\int_0^{2\pi} (4(\beta_N^0(d_c))^2 |V_{N,0}^{l_p}|^2 + f^{(1)}[\beta_n^m]) e^{im\phi}d\phi \tag{13}$$

The right hand side integral in Equation 13 is a linear set of equations in a pair of orthogonal basis: $\Psi_{m,n}^{l_p}$ and $\chi_{m,n}^{l_p}$. $\Psi_{m,n}^{l_p}$ and $\chi_{m,n}^{l_p}$ are essentially modal functions $V_{n,m}^{l_p}$ normalized with the dominant aberration mode $V_{N,0}^{l_p}$. The Riaud method solves Equation 13 by projecting both sides onto these aberration basis $\Psi_{m,n}^{l_p}$ and $\chi_{m,n}^{l_p}$ using inner products. Writing out the solution very generally:

$$(\Psi_{meas}^m, \Psi_{m,n'}^{l_p}) = \mu^{l_p}[\beta_n^m](\Psi_{m,n}^{l_p}, \Psi_{m,n'}^{l_p}) \tag{14}$$

$$(\Psi_{meas}^m, \chi_{m,n'}^{l_p}) = \mu^{l_p}[\beta_n^m](\chi_{m,n}^{l_p}, \chi_{m,n'}^{l_p}) \tag{15}$$

Where the parentheses indicates a inner product defined by:

$$(A_{l_p}, B_{l_p}) = \frac{1}{2|l_p|} \sum_{-|l_p|}^{+|l_p|} \int_0^{+\infty} A_{l_p} \cdot B_{l_p}^* r dr \tag{16}$$

Where the inputs A_{l_p} and B_{l_p} are topological charge value dependent. The aim of the Riaud method is to retrieve a collection of complex numbers $\mu[\beta_n^m]$, and each element inside $\mu[\beta_n^m]$ is a linear combination of β_n^m. The exact equation that relates $\mu[\beta_n^m]$ to β_n^m can be found in the Riaud paper and is skipped here.

$$\mu^{l_p}[\beta_n^m] = (\Psi_{m,n}^{l_p}, \Psi_{m,n'}^{l_p})^{-1}(\Psi_{meas}^{l_p,m}, \Psi_{m,n'}^{l_p}) \tag{17}$$

$$\mu^{l_p}[\beta_n^m] = (\chi_{m,n}^{l_p}, \chi_{m,n'}^{l_p})^{-1}(\Psi_{meas}^{l_p,m}, \chi_{m,n'}^{l_p}) \tag{18}$$

Here the equations are written out for each n,m mode of Zernike. In actual implementation, since we are interested in representing the pupil plane electric field with a number of Zernike modes, equation 17 is a matrix calculation.

3.2 Implementation of the Riaud Method

We use an optical simulation package called "piccsim"[11] specifically for PICTURE-C and PICTURE-D to generate our polarization measurement images. Each image corresponds to a particular $\Psi_{meas}^{l_p,m}$ solution. For each m value, a set of complex numbers $\mu^{l_p}[\beta_n^m]$ is determined through the matrix version of equation 17:

$$\begin{bmatrix} \mu_{0,m}^{l_p} \\ \vdots \\ \mu_{n,m}^{l_p} \\ \vdots \\ \mu_{n_{max},m}^{l_p} \end{bmatrix} = \begin{bmatrix} (\Psi_{0,m}^{l_p}, \Psi_{0,m}^{l_p}) & \cdots & (\Psi_{0,m}^{l_p}, \Psi_{j,m}^{l_p}) & \cdots & (\Psi_{0,m}^{l_p}, \Psi_{n'_{max},m}^{l_p}) \\ \vdots & \ddots & \vdots & \vdots & \vdots \\ (\Psi_{n,m}^{l_p}, \Psi_{0,m}^{l_p}) & \cdots & (\Psi_{n,m}^{l_p}, \Psi_{n',m}^{l_p}) & \cdots & (\Psi_{n,m}^{l_p}, \Psi_{n'_{max},m}^{l_p}) \\ \vdots & \vdots & \vdots & \ddots & \vdots \\ (\Psi_{n_{max},m}^{l_p}, \Psi_{0,m}^{l_p}) & \cdots & (\Psi_{n_{max},m}^{l_p}, \Psi_{n',m}^{l_p}) & \cdots & (\Psi_{n_{max},m}^{l_p}, \Psi_{n'_{max},m}^{l_p}) \end{bmatrix}^{-1} \begin{bmatrix} (\Psi_{meas}^{l_p,m}, \Psi_{0,m}^{l_p}) \\ \vdots \\ (\Psi_{meas}^{l_p,m}, \Psi_{n',m}^{l_p}) \\ \vdots \\ (\Psi_{meas}^{l_p,m}, \Psi_{n'_{max},m}^{l_p}) \end{bmatrix} \tag{19}$$

$$\begin{bmatrix} \mu_{0,m}^{l_p} \\ \vdots \\ \mu_{n,m}^{l_p} \\ \vdots \\ \mu_{n_{max},m}^{l_p} \end{bmatrix} = \begin{bmatrix} (\chi_{0,m}^{l_p}, \chi_{0,m}^{l_p}) & \cdots & (\chi_{0,m}^{l_p}, \chi_{j,m}^{l_p}) & \cdots & \chi_{0,m}^{l_p}, \chi_{n'_{max},m}^{l_p}) \\ \vdots & \ddots & \vdots & \vdots & \vdots \\ (\chi_{n,m}^{l_p}, \chi_{0,m}^{l_p}) & \cdots & (\chi_{n,m}^{l_p}, \chi_{n',m}^{l_p}) & \cdots & (\chi_{n,m}^{l_p}, \chi_{n'_{max},m}^{l_p}) \\ \vdots & \vdots & \vdots & \ddots & \vdots \\ (\chi_{n_{max},m}^{l_p}, \chi_{0,m}^{l_p}) & \cdots & (\chi_{n_{max},m}^{l_p}, \chi_{n',m}^{l_p}) & \cdots & (\chi_{n_{max},m}^{l_p}, \chi_{n'_{max},m}^{l_p}) \end{bmatrix}^{-1} \begin{bmatrix} (\Psi_{meas}^{l_p,m}, \chi_{0,m}^{l_p}) \\ \vdots \\ (\Psi_{meas}^{l_p,m}, \chi_{n',m}^{l_p}) \\ \vdots \\ (\Psi_{meas}^{l_p,m}, \chi_{n'_{max},m}^{l_p}) \end{bmatrix} \tag{20}$$

Which are equivalent to:

$$\mu = G^{-1} r \tag{21}$$

Here the matrix G is the an n by n (a dummy variable n' is used to denote the difference between two n index) matrix that consists of inner products $(\Psi_{m,n}^{l_p}, \Psi_{m,n'}^{l_p})$ and $(\chi_{m,n}^{l_p}, \chi_{m,n'}^{l_p})$. The r vectors consist of the inner products of $(\Psi_{meas}^{l_p,m}, \Psi_{m,n'}^{l_p})$ and $(\Psi_{meas}^{l_p,m}, \chi_{m,n'}^{l_p})$, where $\Psi_{meas}^{l_p,m}$ is the polar Fourier transform of the measurement images.

The exact form of equation 19 and 20 depends on the value of index m. Here we only display the general form above that is conceptually correct. To further retrieve for β_n^m, the coefficient that corresponds to the dominant aberration mode n = N, m = 0 needs to be determined first, which is simply given by the N indexed element for the $\mu[\beta_n^0]$:

Figure 5. Examples of output images. Images are in opposite polarization states. An random error is injected and propagated through the optical simulation to get these output images.

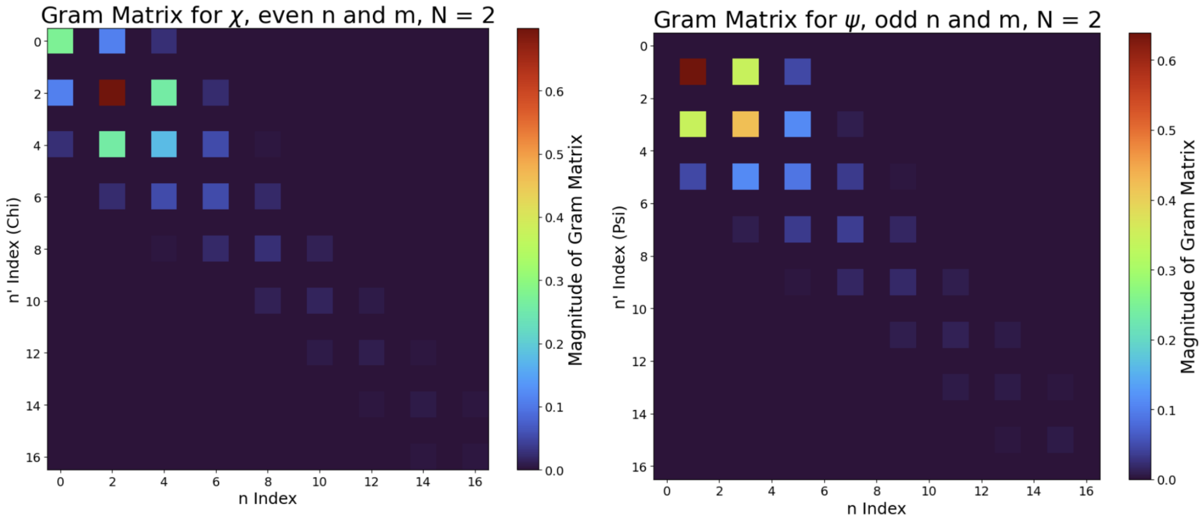

Figure 6. Gram matrices befrore inversion. These are visualized results of inner products shown in equation 19 and equation 20. Left: $(\Psi^{lp}_{m,n}, \Psi^{lp}_{m,n'})$ Right: $(\chi^{lp}_{m,n}, \chi^{lp}_{m,n'})$ Please note that the Gram matrix associated with $\Psi^{lp}_{m,n}$ is only nonzero for odd n and m index, and Gram matrix associated with $\chi^{lp}_{m,n}$ is only nonzero for even n and m index.

$$\mu[\beta^0_n] = \begin{bmatrix}\mu[\beta^0_0] & \cdots & \frac{1}{2}(\beta^0_N)^2 & \cdots & \mu[\beta^0_{n_{max}}]\end{bmatrix} \tag{22}$$

Where $\frac{1}{2}(\beta^0_N)^2$ corresponds to $\mu[\beta^0_0]$. Using the relation $\beta^0_N = \sqrt{2\mu[\beta^0_0]}$, β^0_N is retrieved as the first complex coefficients. Using thie coefficient, the other complex β^m_n can be retrieved from the array $\mu[\beta^m_n]$. Due to the complexity of the exact math, the steps to retrieve rest of the complex coefficients are skipped.

3.3 Testing The Riaud Method

We implemented the Riaud method in python with the above mentioned steps over the polarized measurement image and were able to retrieve β^m_n coefficeints. To validate out results, we use the retrieved coefficients to reconstruct the pupil plane electric field and we compare the reconstructed field with the input field. Please note here that we are not directly comparing the coefficient value with the input Zernike mode values, as there might be presence of cross talk between each mode.

As previously mentioned the measurement images consists of circular polarizations in both handedness, and an unpolarized image. The simulated optical system follows the conceptual layout in 1. In the optical simulation, We use deformable mirrors to input pupil plane phase and amplitude aberrations in terms of Zernike modes.

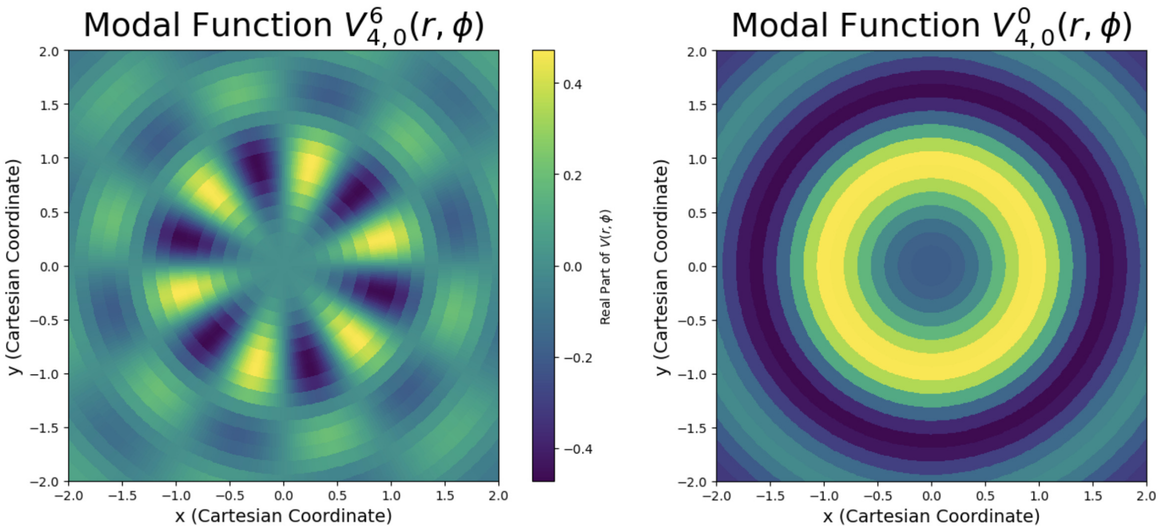

Figure 7. Modal functions for $l_p = 0$ and $l_p = 6$. We use m = 0 and n = 4 to generate these example images. These Modal functions display features that are similar to what circularly polarized light ($l_p \neq 0$) and unpolarized light ($l_p = 0$) experience at the focal plane of VVC.

The output images are in both orthogonal linear polarization states. Example of the pair of output images can be seen in Figure 5.

For each retrieval, a certain number of Zernike polynomials are used to construct the base. The total number of Zernike modes are determined by the n index. We used n = 16 for our retrieval, which leads to a total number of 136 Zernike Modes. Our python implementation follows the Riaud method to create the following functions and calculations:

1. The Modal Function $V^{l_p}_{n,m}$. Figure 7
2. The polar Fourier Transform of the measurement images: $\Psi^{l_p,m}_{meas}$
3. The G Matrix and its inverse. These are inner products between aberration templates: $(\Psi^{l_p}_{m,n}, \Psi^{l_p}_{m,n'})$ and $(\chi^{l_p}_{m,n}, \chi^{l_p}_{m,n'})$. Figure 6 shows example of these matrices before inversion.
4. The r vectors. These are inner products between the polar Fourier transformed images and the aberration template: $(\Psi^{l_p,m}_{meas}, \Psi^{l_p}_{m,n'})$ and $(\Psi^{l_p,m}_{meas}, \chi^{l_p}_{m,n'})$
5. The math to retrieve β^m_n from $\mu[\beta^m_n]$

3.4 Results from our implementation

Through our implementation we noticed that the reconstructed electric field does not match with the input electric field. In following sections we examine different aspects of our implementation and of the Riaud method itself.

3.4.1 Constructing the pupil plane electric field using $P(\rho,\theta) = \sum(Re(\beta^m_n) + Im(\beta^m_n))Z^m_n$

The first aspect we examined was the validity of using $P(\rho,\theta) = \sum(Re(\beta^m_n) + Im(\beta^m_n))Z^m_n$ to represent the pupil plane electric field. We tried to justify if it is possible to retrieve electric field in the form of $P(\rho,\theta) = \sum(Re(\beta^m_n) + Im(\beta^m_n))Z^m_n$ by performing a Fourier transform on any aberrated wavefront represented by an electric field, using the following equation:

$$\beta^m_n = \frac{1}{|Z^m_n|^2} \int_{y_{min}}^{y_{max}} dy \int_{x_{min}}^{x_{max}} dx \cdot P(x,y) Z^m_n \tag{23}$$

Where the pupil function $P(x, y)$ follows the definition from equation 6, except now in cartesian coordinates. The cartesian coordinate is chosen for simplicity of applying python's built-in Fourier transform function. Our

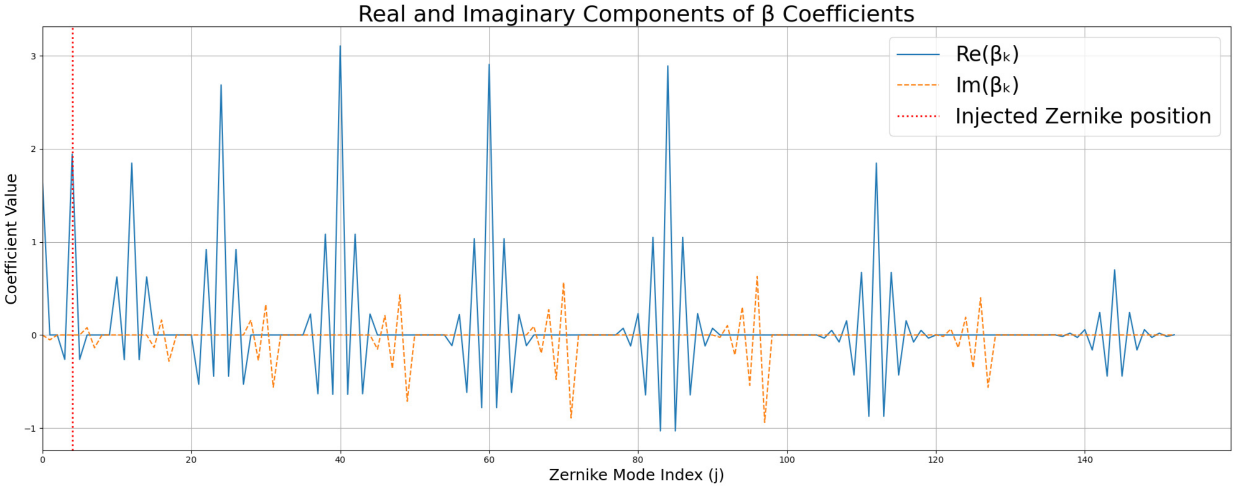

Figure 8. retrieved $Re(\beta_n^m)$ and $Im(\beta_n^m)$ as a function of the j index, following the ANSI standard definition. The injected error in the input field is at Z_2^0. We notice that the retrieved coefficients are always real or imaginary, which is confirmed in our appendix A. We notice also that all the radial modes coefficients with m = 0 has significant contribution to the retrieval, regardless of the actual mode injected.

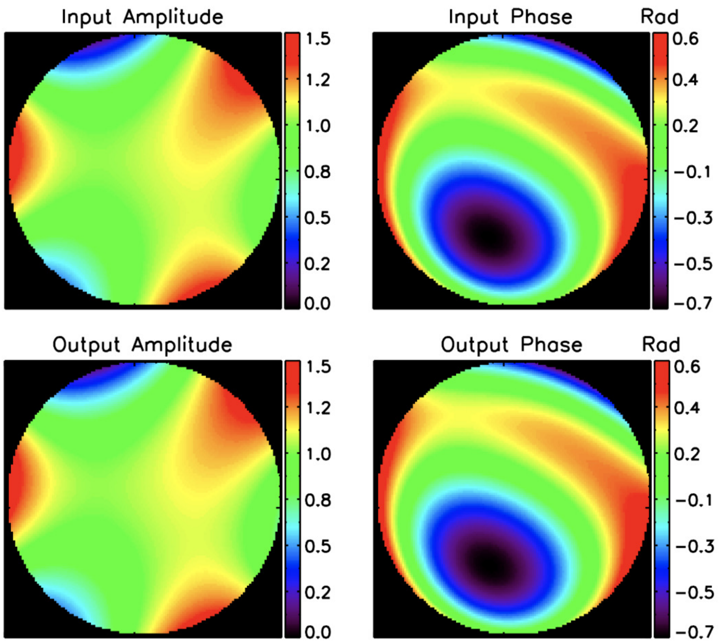

Figure 9. Comparison between input field and retrieved field in phase and amplitude An random error is injected to aberrate the input field. We use equation 23 on the input field to retrieve complex β_n^m coefficients, and then use these coefficients to reconstruct the field. 10 Zernike polynomials are used to construct the aberrated wavefront, while 100 Zernike polynomials are used for the reconstruction. The output field, which is the reconstructed, is almost identical with the input field.

attempt (Figure 9) at using this method of retrieval showed that it is entirely possible to retrieve and reconstruct pupil plane electric field with complex β_n^m. We noticed that in the case of single error injection, meaning a particular Zernike mode is chosen to be injected, aside from the presence of some other nonzero β_n^m, the coefficient that corresponds directly to the injected error tends to be dominant.

3.4.2 β_n^m is either real or imaginary, never complex

Another thing we noticed from our retrieval is that the retrieved complex beta coefficient is either real or imaginary, but never complex, as can be seen in Figure 8. Upon reviewing the math from Riaud method we proved that this is indeed the case: β_n^m is limited to be either real or imaginary. Furthermore, within an n index group, meaning all Zernike polynomials with the same n number, β_n^m is only real or only imaginary. The derivation is demonstrated in appendix A

It is still possible to have reconstructed field that are composed of real and imaginary β_n^m coefficients. However another limitation we noticed in appendix A is that the parity of n and m determines whether the resulting β_n^m coefficients will be real or imaginary, therefore we noticed this alternating order of real and imaginary numbers (need a plot here). This indicates that within an n index, all β_n^m will be real only or imaginary only.

3.4.3 Dominant aberration β_N^0 is radial

Paying closer attention to the choice of β_N^0 we notice that this mode of aberration is always radial, as all m = 0 Zernike polynomials, are related a defocus/radial mode aberrations. We also noticed in our retrieval that, regardless the wavefront errors we injected are radial or not radial, the β_n^m coefficients related to these m = 0 modes are always dominant. This seems to contradict what we noticed in section 3.4.1, where the retrieved dominant coefficients should correspond to the wavefront error injected. For example, if a single vertical coma (m = 1, n =3) is injected, then in the retrieved coefficients, using the Fourier transform method presented in section 3.4.1, the dominant aberration among all coefficients should be β_3^1.

4 Conclusion: Summary of current progress and what's next

In this article we present our progress in making a polarimeter for the PICTURE-D optics. Our polarimeter demo demonstrated that it is capable of taking Stokes polarization measurement. For future flight we aim to integrate the polarimeter modality into PICTURE-D modality. Simulations will be performed to ensure we can achieve optimal contrast measurement and polarization measurement simultaneously.

We also attempted to implement the Riaud method to perform polarization based wavefront sensing in simulation. However, from our results, we notice there are limitations to the method, although the assumption of retrieving wavefront aberration over a pupil plane electric field construction of $P(\rho, \theta) = \sum (Re(\beta_n^m) + Im(\beta_n^m)) Z_n^m$ is valid.

ACKNOWLEDGMENTS

This Work is funded by NASA APRA Grant 80NSSC22K1648. I would like to thank Chris Mendillo for the support and useful discussions during the project. I would also like to thank our collaborator David Doelman and our colleague Sunip Mukherjee for their time and insightful inputs. Special thanks to Orban de xivry Gilles and David Mawet for helpful correspondence and meeting.

REFERENCES

[1] et.al, E., "Debris disk results from the gemini planet imager exoplanet survey's polarimetric imaging campaign," *The Astronomical Journal* (2020).
[2] et.al, V., "Polarization of stars with debris discs: comparing observations with models," *Monthly Notices of the Royal Astronomical Society* (2019).
[3] Give'on, A., Kern, B. D., and Shaklan, S., "Pair-wise, deformable mirror, image plane-based diversity electric field estimation for high contrast coronagraphy," in [*Techniques and Instrumentation for Detection of Exoplanets V*], **8151**, 376–385, SPIE.
[4] Riaud, P., Mawet, D., and Magette, A., "Instantaneous phase retrieval with the vector vortex coronagraph -theoretical and optical implementation," **545**, A151. Publisher: EDP Sciences.
[5] Doelman, D. S., Por, E. H., Ruane, G., Escuti, M. J., and Snik, F., "Minimizing the polarization leakage of geometric-phase coronagraphs with multiple grating pattern combinations," **132**(1010), 045002.

[6] Doelman, D. S., Snik, F., Por, E. H., Bos, S. P., Otten, G. P. P. L., Kenworthy, M., Haffert, S. Y., Wilby, M., Bohn, A. J., Sutlieff, B. J., Miller, K., Ouellet, M., De Boer, J., Keller, C. U., Escuti, M. J., Shi, S., Warriner, N. Z., Hornburg, K., Birkby, J. L., Males, J., Morzinski, K. M., Close, L. M., Codona, J., Long, J., Schatz, L., Lumbres, J., Rodack, A., Van Gorkom, K., Hedglen, A., Guyon, O., Lozi, J., Groff, T., Chilcote, J., Jovanovic, N., Thibault, S., De Jonge, C., Allain, G., Vallée, C., Patel, D., Côté, O., Marois, C., Hinz, P., Stone, J., Skemer, A., Briesemeister, Z., Boehle, A., Glauser, A. M., Taylor, W., Baudoz, P., Huby, E., Absil, O., Carlomagno, B., and Delacroix, C., "Vector-apodizing phase plate coronagraph: design, current performance, and future development [invited]," **60**(19), D52.

[7] Mawet, D., Serabyn, E., Liewer, K., Hanot, C., McEldowney, S., Shemo, D., and O'Brien, N., "Optical vectorial vortex coronagraphs using liquid crystal polymers: theory, manufacturing and laboratory demonstration," **17**(3), 1902.

[8] Mendillo, C. B., Hewawasam, K., Martel, J., Cook, T. A., Chakrabarti, S., Snik, F., and Doelman, D., "Dual-polarization electric field conjugation and applications for vector vortex coronagraphs," in [*Techniques and Instrumentation for Detection of Exoplanets X*], **11823**, 586–594, SPIE.

[9] Chipman, R. A., Lam, W.-S. T., and Young, G., [*Polarized light and optical systems*], Optical sciences and applications of light, CRC Press.

[10] Snik, F., Otten, G., Kenworthy, M., Miskiewicz, M., Escuti, M., Packham, C., and Codona, J., "The vector-APP: a broadband apodizing phase plate that yields complementary PSFs," 84500M.

[11] Mendillo, C. B., Howe, G. A., Hewawasam, K., Martel, J., Finn, S. C., Cook, T. A., and Chakrabarti, S., "Optical tolerances for the PICTURE-c mission: error budget for electric field conjugation, beam walk, surface scatter, and polarization aberration," in [*Techniques and Instrumentation for Detection of Exoplanets VIII*], Shaklan, S., ed., 34, SPIE.

A Appendix: β Coefficient is Either Real or Imaginary

The goal of this appendix is to examine if the coefficient β_n^m remains complex throughout the retrieval process. To retrieve for β_n^m coefficients, a set of $\mu[\beta_n^m]$ needs to be retrieved from:

$$\mu[\beta_n^m] = G^{-1}r \tag{24}$$

Where the Gram matrix G are inner products of the forms: $(\Psi_{m,n}^{l_p}, \Psi_{m,n'}^{l_p})$ and $(\chi_{m,n}^{l_p}, \chi_{m,n'}^{l_p})$. The r vectors are inner products of the forms: $(\Psi_{meas}^{l_p,m}, \Psi_{m,n'}^{l_p})$ and $(\Psi_{meas}^{l_p,m}, \chi_{m,n'}^{l_p})$, where $\Psi_{meas}^{l_p,m}$ is the polar Fourier transform of the measurement images.

The aberration basis $\Psi_{n,m}^{l_p}(r, l_p)$ and $\chi_{n,m}^{l_p}(r, l_p)$ are defined as:

$$\Psi_{n,m}^{l_p}(r, l_p) = -8\epsilon_m^{-1}\mathrm{Im}(i^m V_{n,m}^{l_p} \cdot V_{N,0}^{l_p *}) \tag{25}$$

$$\chi_{n,m}^{l_p}(r, l_p) = 8\epsilon_m^{-1}\mathrm{R}(i^m V_{n,m}^{l_p} \cdot V_{N,0}^{l_p *}) \tag{26}$$

Where the modal function $V_{n,m}^{l_p}$ is defined as:

$$V_{n,m}^{l_p}(r, \phi) = \epsilon_{l_p}(-1)^{\frac{n+m}{2}} \frac{J_{n+1}(2\pi r)}{2\pi r} e^{il_p\phi} \tag{27}$$

The value of ϵ_{l_p} depends on the topological charge l_p and the value of ϵ_m depends on m:

$$\epsilon_{l_p} = -i, l_p \neq 0 \qquad \epsilon_{l_p} = 1, l_p = 0 \tag{28}$$

$$\epsilon_m = 2, m \neq 0 \qquad \epsilon_m = 1, m = 0 \tag{29}$$

Both aberration templates depend on the value of dot product $V_{n,m}^{l_p} \cdot V_{N,0}^{l_p *}$. This behaviour is confirmed in the following section. A closer look at this dot product we can see that no matter what value of the topological charge l_p is, the result of the dot product is always real. This is demonstrated in the following calculation:

$l_p = 6$**,** ϵ_{l_p} **= -i**

$$\begin{aligned} V_{n,m}^{l_p} \cdot V_{N,0}^{l_p *} &= \epsilon_{l_p}(-1)^{\frac{n+m}{2}} \frac{J_{n+1}(2\pi r)}{2\pi r} e^{il_p\phi} \cdot [\epsilon_{l_p}(-1)^{\frac{N}{2}} \frac{J_{n+1}(2\pi r)}{2\pi r} e^{il_p\phi}]^* \\ &= (-1)^{\frac{n+m+N}{2}} [\frac{J_{n+1}(2\pi r)}{2\pi r}]^2 (-i)(i) \\ &= (-1)^{\frac{n+m+N}{2}} [\frac{J_{n+1}(2\pi r)}{2\pi r}]^2 \qquad \text{(Result is Real)} \end{aligned}$$

$l_p = 0$**,** ϵ_{l_p} **= 1**

$$V_{n,m}^{l_p} \cdot V_{N,0}^{l_p *} = (-1)^{\frac{n+m+N}{2}} [\frac{J_{n+1}(2\pi r)}{2\pi r}]^2 \qquad \text{(Result is Real)}$$

The fact that $V_{n,m}^{l_p} \cdot V_{N,0}^{l_p *}$ is always real implies that:

$\Psi_{n,m}^{l_p}(r, l_p) = 0$ when m is even, since $i^m V_{n,m}^{l_p} V_{N,0}^{l_p *}$ is **real** for even m

$\chi_{n,m}^{l_p}(r, l_p) = 0$ when m is odd, since $i^m V_{n,m}^{l_p} V_{N,0}^{l_p *}$ is **imaginary** for odd m

Now, going back to the equation $\mu[\beta_n^m] = G^{-1} r$:

r Vectors

$$\begin{aligned} r(\chi) &= (\Psi_{\text{meas}}^m, \chi_{n,m}^{l_p}) \\ r(\Psi) &= (\Psi_{\text{meas}}^m, \Psi_{n,m}^{l_p}) \end{aligned}$$

G Matrix

$$\begin{aligned} G(\chi) &= (\chi_{n,m}^{l_p}, \chi_{n,m}^{l_p}) \\ G(\Psi) &= (\Psi_{n,m}^{l_p}, \Psi_{n,m}^{l_p}) \end{aligned}$$

The result from the previous section reveals that for $G(\chi)$ and $G(\Psi)$:

$$\begin{aligned} G(\Psi) = (\Psi_{n,m}^{l_p}, \Psi_{n,m}^{l_p}) = 0 \qquad & \text{when m is even.} \\ G(\chi) = (\chi_{n,m}^{l_p}, \chi_{n,m}^{l_p}) = 0 \qquad & \text{when m is odd.} \end{aligned}$$

Without writing out the explicit form of $\mu[\beta_n^m]$ in all scenarios, each $\mu[\beta_n^m]$ is composed directly of complex numbers A_c^m, A_s^m,B_c^m, B_s^m.Where the A and B coefficients are defined as:

$$A_c^m = \text{R}(\beta_N^0)\text{R}(\beta_{cn}^m) + \text{Im}(\beta_N^0)\text{Im}(\beta_{cn}^m) \tag{30}$$

$$B_c^m = \text{R}(\beta_N^0)\text{Im}(\beta_{cn}^m) - \text{Im}(\beta_N^0)\text{R}(\beta_{cn}^m) \tag{31}$$

$$A_s^m = \text{R}(\beta_N^0)\text{R}(\beta_{sn}^m) + \text{Im}(\beta_N^0)\text{Im}(\beta_{sn}^m) \tag{32}$$

$$B_s^m = \text{R}(\beta_N^0)\text{Im}(\beta_{sn}^m) - \text{Im}(\beta_N^0)\text{R}(\beta_{sn}^m) \tag{33}$$

Where subscripts of s and c corresponds to odd sine modes and even cosine modes. The coefficient that corresponds to the dominant aberration mode n = N, m = 0 is given by the N indexed element for the $\mu[\beta_n^0]$:

$$\mu[\beta_n^0] = \begin{bmatrix} \mu[\beta_0^0] & \cdots & \frac{1}{2}(\beta_N^0)^2 & \cdots & \mu[\beta_{n_{max}}^0] \end{bmatrix} \tag{34}$$

Where $\frac{1}{2}(\beta_N^0)^2$ corresponds to $\mu[\beta_0^0]$. Using the relation $\beta_N^0 = \sqrt{2\mu[\beta_0^0]}$, β_N^0 can be retrieved. This coefficient can then be used to solve for other β_n^m.

There are three different definition of $\mu[\beta_n^m]$: The general case $\mu[\beta_n^m]$ with m $<$ n, and two other special cases of $\mu[\beta_n^0]$ m $=$ 0 and $\mu[\beta_n^n]$ m $=$ n. Each of this definition is composed of different linear combinations of A_c^m, A_s^m,B_c^m, and B_s^m. Writing these cases out explicitly:

- $m = 0$

$$\mu[A] = \overset{\sim}{\sum_n} A_c^0(n) + \frac{1}{2}{\beta_N^0}^2 = (\chi_{n,0}^{l_p}, \chi_{n',0}^{l_p})^{-1}(\Psi_{\text{meas}}^0, \chi_{n',0}^{l_p}) \tag{35}$$

$$\mu[B] = B_c^0(n) = (\Psi_{n,0}^{l_p}, \Psi_{n',0}^{l_p})^{-1}(\Psi_{\text{meas}}^0, \Psi_{n',0}^{l_p}) \tag{36}$$

- $m < n$

$$\mu[A] = \sum_n A_c^m(n) + iA_s^m(n) = (\chi_{n,m}^{l_p}, \chi_{n,m}^{l_p})^{-1}(\Psi_{\text{meas}}^m, \chi_{n,m}^{l_p}) \tag{37}$$

$$\mu[B] = \sum_n B_c^m(n) + iB_s^m(n) = (\Psi_{n,m}^{l_p}, \Psi_{n,m}^{l_p})^{-1}(\Psi_{\text{meas}}^m, \Psi_{n,m}^{l_p}) \tag{38}$$

- $m = n$

$$\mu[A] = \sum_n([A_c^m(n) + A_s^m(n)] + i * \text{Sign}(l_p)[A_c^n(n) - A_s^n(n)]) = (\chi_{n,n}^{l_p}, \chi_{n',n}^{l_p})^{-1}(\Psi_{\text{meas}}^n, \chi_{n,m}^{l_p}) \tag{39}$$

$$\mu[B] = \sum_n([B_c^m(n) + B_s^m(n)] + i * \text{Sign}(l_p)[B_c^m(n) - B_s^m(n)]) = (\Psi_{n,m}^{l_p}, \Psi_{n',n}^{l_p})^{-1}(\Psi_{\text{meas}}^m, \Psi_{n',n}^{l_p}) \tag{40}$$

Where the subscript c indicates even Zernike mode ($m \geq 0$), and s indicate odd Zernike mode ($m < 0$). As mentioned before, when m and n are odd, $(\chi_{n,m}^{l_p}, \chi_{n,m}^{l_p}) = 0$; when m and n are even, $(\Psi_{n,m}^{l_p}, \Psi_{n,m}^{l_p}) = 0$.This means we can solve only for $\mu[A]$ when n and m are odd, or only for $\mu[B]$ when n and m are even.

Looking at the expressions for $\mu[\beta_n^m]$, we can see that the retrieval of β_n^m depends on coefficients A and B, which are real numbers. Now we examine the retrieval of β_n^m from the A and B coefficients.Looking at the expressions for A_c^m and A_s^m:

$$A_c^m = \text{R}(\beta_N^0)\text{R}(\beta_{cn}^m) + \text{Im}(\beta_N^0)\text{Im}(\beta_{cn}^m) \tag{41}$$

$$A_s^m = \mathrm{R}(\beta_N^0)\mathrm{R}(\beta_{sn}^m) + \mathrm{Im}(\beta_N^0)\mathrm{Im}(\beta_{sn}^m) \tag{42}$$

If β_N^0 is complex, it is impossible to solve for β_n^m. However, the solution of β_N^0 is given by:

$$(\Psi_{meas}^0, \chi_{n',0}^{l_p}) = \frac{1}{2}(\beta_N^0)^2(\chi_{N,0}^{l_p}, \chi_{n',0}^{l_p}) + \sum_n A_c^0(n)(\chi_{n,0}^{l_p}, \chi_{n',0}^{l_p}) \tag{43}$$

Where the polar Fourier transform is defined by:

$$\Psi_{meas}^m(r, l_p) = \frac{1}{2\pi}\int_0^{2\pi} I_{meas}(r, \phi, l_p)e^{im\phi}d\phi \tag{44}$$

From expressions above: Ψ^0_{meas} is real since m = 0, and the Image intensity only has real value in each pixel. $\chi_{n,m}^{l_p}$ is real, this means the entire array of $u[\beta_n^0]$ is composed of real numbers, which means β_N^0 is either real or imaginary, but not complex. This means that we can only retrieve for $R(\beta)$ or $Im(\beta)$

Now if we look at the coefficients B:

$$B_c^m = \mathrm{R}(\beta_N^0)\mathrm{Im}(\beta_{cn}^m) - \mathrm{Im}(\beta_N^0)\mathrm{R}(\beta_{cn}^m) \tag{45}$$

$$B_s^m = \mathrm{R}(\beta_N^0)\mathrm{Im}(\beta_{sn}^m) - \mathrm{Im}(\beta_N^0)\mathrm{R}(\beta_{sn}^m) \tag{46}$$

Similarly, we can only retrieve for $R(\beta)$ or $Im(\beta)$, which means that when we solve for β_{cn}^m and β_{sn}^m we will only get a real solution or an imaginary solution, but never complex. Furthermore, when β_N^0 is real, we can only retrieve $\mathrm{R}(\beta_{cn}^m)$ and $\mathrm{R}(\beta_{sn}^m)$ for even m and n from A coefficients, as A is associated with $(\chi_{n,n}^{l_p}, \chi_{n',n}^{l_p})$, which is nonzero only for even n and m. When β_N^0 is imaginary, we can only retrieve $\mathrm{R}(\beta_{cn}^m)$ and $\mathrm{R}(\beta_{sn}^m)$ for odd m and n from B coefficeints, as B is associated with $(\Psi_{n,n}^{l_p}, \Psi_{n',n}^{l_p})$, which nonzero only for odd n and m. This observation explains the alternating behaviour we observed in Figure 8.